Photon-magnon coupling using gain-assisted spoof-localized surface plasmons

YUZAN XIONG,[1] ANDREW CHRISTY,[1,2] YI LI,[3] RUI SUN,[4] ANDREW H. COMSTOCK,[4] JUNMING WU,[1] RENE LOPEZ,[1] SIDONG LEI,[5,6] DALI SUN,[4] JAMES F. CAHOON,[2] XUFENG ZHANG,[7,8] BINBIN YANG,[9,*] AND WEI ZHANG,[1,*]

[1]*Department of Physics and Astronomy, University of North Carolina at Chapel Hill, Chapel Hill, NC 27599, USA*
[2]*Department of Chemistry, University of North Carolina at Chapel Hill, Chapel Hill, NC 27599, USA*
[3]*Materials Science Division, Argonne National Laboratory, Argonne, IL 60439, USA*
[4]*Department of Physics and Organic and Carbon Electronics Lab (ORaCEL), North Carolina State University, Raleigh, NC 27695, USA*
[5]*NanoScience Technology Center, University of Central Florida, Orlando, FL 32826, USA*
[6]*Department of Material Science and Engineering, University of Central Florida, Orlando, FL 32816, USA*
[7]*Department of Electrical and Computer Engineering, Northeastern University, Boston, MA 02115, USA*
[8]*Department of Physics, Northeastern University, Boston, MA 02115, USA*
[9]*Department of Electrical and Computer Engineering, North Carolina A&T State University, Greensboro, NC 27411, USA*
[*]*byang1@ncat.edu*
[*]*zhwei@unc.edu*

Abstract: Improving the photon-magnon coupling strength can be done by tuning the structure of microwave resonators to better interact with the magnon counterpart. Planar resonators accommodating unconventional photon modes beyond the half- and quarter-wavelength designs have been explored due to their optimized mode profiles and potentials for on-chip integration. Here, we designed and fabricated an actively controlled ring resonator supporting the spoof localized surface plasmons (LSPs), and implemented it in the investigation of photon-magnon coupling for hybrid magnonic applications. We demonstrated gain-assisted photon-magnon coupling with the YIG magnon mode under several different sample geometries. The achieved coupling amplification is largely benefited from the high quality factor (Q-factor) due to the additional gain provided by a semiconductor amplifier, which effectively increases the Q-factor from a nearly null state (passive resonance) to more than 1000 for a quadrupole LSP mode. Our results suggest an additional control knob for manipulating photon-magnon coupled systems exploiting external controls of gain and loss.

1. Introduction

Hybrid magnonic systems are promising modular components for quantum transduction and sensing applications owing to their capability of connecting distinct quantum platforms [1]. Strong and coherent hybridization of magnons with phonons, microwave photons, and optical light have been demonstrated, with the observation of characteristic phenomena that bestow emerging quantum engineering functionalities [2–6].

Among the various systems, the photon-magnon hybridization [7, 8] remains the primary testbed for exploring many coherent phenomena emerging from hybrid magnonics, such as coherent [9–11] and dissipative [12, 13] couplings, nonreciprocal transmission [14, 15], remote communication [16–18], magnetically-induced transparency [19–21], super-strong coupling [22], zero-reflection [23], and *PT*-symmetric singularities [24, 25]. These numerous coupling manifestations have largely benefited from the capability of engineering the tailored modes, in which two most prominent engineering tasks are 'mode-profile manipulation' and 'mode amplification', and they apply to both the photon and magnon counterparts.

On the magnon side, the mode profiles can be tuned via excitation schemes [26], external magnetic field [20, 27], and size and geometry of the magnet (including nanostructured samples) [28]. The amplification of magnons, however, has been recognized as a long-standing challenge [5], but recent progresses have indicated promising solutions via engineering the combined spatial and temporal magnon profiles [29, 30]. On the photon side, new microwave resonator designs, especially in the planar geometry [7], have been studied for improved quality factors (Q-factors) and mode profiles dedicated to photon-magnon systems. For example, diabolo cavity [31], dark mode resonance [32], spiral resonator [33], and spoof surface plasmons [34] have been designed and implemented beyond conventional stripline [35] or lumped types [36]. For amplification of photon modes, additional semiconductor gain [37] or feedback loops [38, 39] can be incorporated, as have been recently demonstrated to support novel gain-driven magnon polaritons [40, 41] and long-distance photon-magnon coherence [42].

Due to the near-field nature of the photon-magnon coupling, the microwave surface plasmon mode [43] is one of the most intriguing candidates, which offers simultaneously a rich variety of mode profiles and superior Q-factors. One particularly interesting manifestation pertinent to photon-magnon systems is the spoof-localized surface plasmon (spoof-LSP) modes [44–47], with appealing features such as highly concentrated EM fields near the surface, a weak coupling to radiative waves, deep sub-wavelength excitation, and superior sensitivity to the dielectric environment. These nice properties have made spoof-LSPs favorably adopted in GHz-THz photonics that embrace a wide range of applications [43–50]. Recently, spoof-LSPs have been implemented in photon-magnon coupled systems using a spiral resonator design [51]. The enhanced coupling strength and highly tunable mode profiles have rendered them highly promising contenders for engineering photon-magnon hybrids. However, the possibility of further boosting photon-magnon coupling using actively driven spoof-LSP modes has remained elusive.

In this work, we study a gain-assisted spoof-LSP mode by integrating the resonator with a low-noise amplifier circuit. Instead of using the spiral design, the spoof-LSP resonator is composed of a corrugated ring with a slit to easily incorporate the gain circuit elements. We demonstrate that the Q-factor of the passive resonator is very sensitive to the different magnetic loads placed atop, but can be significantly increased upon applying the gain, and, subsequently lead to an increased photon-magnon coupling strength with a $Y_3Fe_5O_{12}$ (YIG) sphere.

2. Experiment

We integrate the corrugated ring resonator structure in line with a microwave stripline for transmission experiments, as illustrated in Fig.1(a). To enhance the stripline-resonator capacitive coupling, we soldered two additional 15-pF capacitors on the respective ends of the resonator. To incorporate the amplifer chip, a slit has been cut in the corrugated ring, and the solder pads are also fabricated as necessary to support the biasing circuit.

The microwave laminate board is Rogers TMM10i with a metal layer thickness of 35 μm, a total thickness of 1.27 mm, and a relative dielectric constant of the substrate ϵ_r of 9.8. The corrugated ring resonator parameters are listed as follows: the number of grooves $N = 21$, inner radius $r = 5.2$ mm, and the central strip width $g_r = 0.8$ mm. The groove height is $h = 2.25$ mm, the period is $p = 2\pi(r + g_r + h)/N = 2.47$ mm, and the groove width is $a = 0.988$ mm. The gap between the micro-stripline and the grooved ring resonator is $g_m = 0.5$ mm.

The biasing circuit structure, depicted in Fig.1(a), uses metallic pads to mount the lumped components, including capacitors, inductors, and resistors. The amplifier chip is the BGA low-noise amplifier (Infineon), with dimensions 2 mm $\times$ 2.1 mm $\times$ 0.9 mm. The lumped components in the biasing circuit were selected based on the specs of the amplifier chip. The gain of the amplifier chip is controlled by using an external dc voltage, tunable from 0 to 4.1 V. The transmission characteristic of the structure was measured by using a vector-network analyzer (VNA, PicoVNA-106, Pico Technology Ltd).

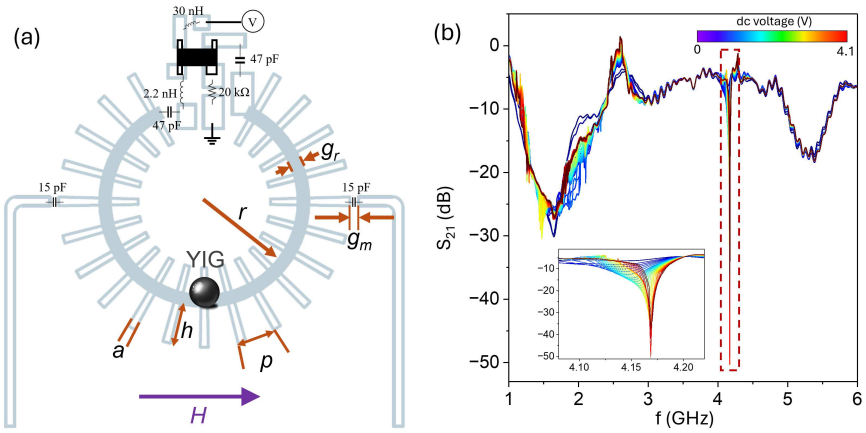

Fig. 1. (a) Resonator design and dimension. The number of grooves $N = 21$, inner radius $r = 5.2$ mm, central strip width $g_r = 0.8$ mm, groove height $h = 2.25$ mm, period $p = 2\pi(r + g_r + h)/N = 2.47$ mm, groove width $a = 0.988$ mm, and gap between the micro-stripline and the grooved ring resonator $g_m = 0.5$ mm. A slit is cut near the top of the resonator, to accommodate the biasing circuit with fabricated solder pads to support the circuit elements. Magnetic loads such as a YIG sphere is placed at the bottom of the corrugated ring for photon-magnon coupling investigations. External magnetic field, H, is applied along the horizontal direction. (b) The S_{21} transmission spectra under varying dc voltage applied to the amplifer (0 to 4.1 V) in the presence of a YIG sphere placed at the bottom of the resonator ring.

3. Results and Discussion

3.1. Spectral and spatial properties of gain-assisted spoof-LSPs

Figure 1(b) shows the measured S_{21} spectra with varying dc voltage applied to the amplifer in the presence of a YIG sphere (whose photon-magnon coupling properties will be discussed later). We observed selective amplification in the transmission spectra close to the eigen-frequencies of the spoof-LSP resonator, i.e. a band localized around 2.2 GHz and 2.6 GHz, as well as a sharp resonance near 4.2 GHz (inset of Fig.1(b)). The mode near 2.6 GHz corresponds to a dipolar mode and the one near 4.2 GHz is a quadrupole mode (details to be discussed later). No significant amplification effect was found for other frequencies in the measured range.

We then focus on the sharp resonance at ~4.2 GHz corresponding to the quadrupole mode. Figure 2(a) and (b) show the dc-voltage dependence of the resonance frequency (f_{res}) and Q-factor, respectively, of such a mode without any YIG load. The f_{res} shifts almost linearly with the dc voltage in the applied dc voltage range. The Q-factor, on the other hand, grows slowly at the beginning (from 3 – 3.5V) but rapidly increases after 3.6V, reaching a Q-factor value exceeding 1,000 at 4.1V.

One notable feature of spoof-LSPs in contrast to common waveguide modes is their high sensitivity to local dielectric environments, which can be readily modified by adding the magnetic load atop the resonator surface. To examine this effect, we tested four $Y_3Fe_5O_{12}$(YIG) samples with various geometries and dimensions. The magnetic loads were all placed at the bottom of the resonator ring, an optimal location that we identified for photon-magnon coupling via a preliminary position test. This coupling sensitivity to sample location has also been demonstrated

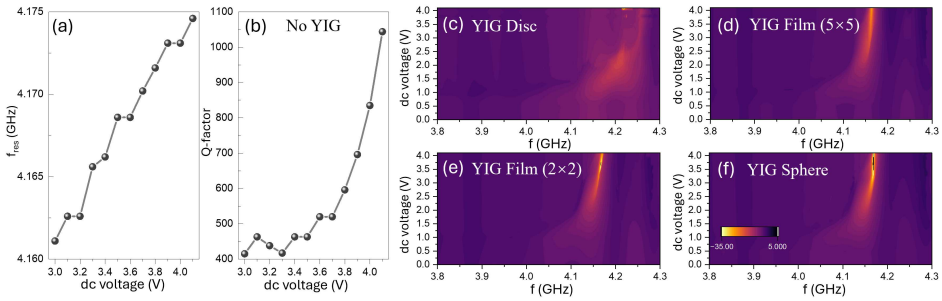

Fig. 2. (a,b) Dc-voltage dependent LSP mode characteristics near 4.2 GHz: (a) Resonator frequency, f_{res}, and (b) Q-factor, without any magnetic load. Contour plot of the S_{21} transmission spectra (dc voltage – frequency) near 4.2 GHz for different YIG loads: (c) YIG disc, 5-mm diameter, (d) YIG film, 5×5 square, (e) YIG film, 2×2 square, and (f) YIG sphere, 1-mm diameter.

in previous reports for similar localized resonator modes [33, 51, 52].

Figure 2(c-f) show the "dc voltage – frequency" contour plots of the S_{21} transmission spectra near the 4.2-GHz mode for different YIG loads: (c) a disc of 5-mm diameter and 350-μm thickness; (d) a thin film of 5×5 mm^2 square and 1-μm thickness; (e) a thick film of 2×2 mm^2 square and 20-μm thickness; (f) a sphere of 1-mm diameter. Notably, the four YIG samples differ in both their thicknesses and the lateral dimensions. By comparing the results of the modified Q-factors due to additional loss, we found that the lateral dimension plays a more critical role than the thickness in the reshaping of the transmission characteristics. The YIG disc, because of both its large thickness and diameter, broadens the resonance profile of the LSP mode at low to intermediate dc voltages, Fig. 2(c), although the resonance sharpens when sufficiently high dc voltage (> 4.0 V) is applied. Compared to the disc, the 5×5 film results in a notable broadening of the mode linewidth; however, the LSP mode resonance profile was still largely maintained, Fig. 2(d). On the other hand, both the 2×2 film, Fig. 2(e), and the sphere, Fig. 2(f), result in only mild linewidth broadening due to their smaller lateral sizes, despite their larger thicknesses. This observation can be explained by considering the spatial profile of the LSP mode, which is typically highly surface localized, but decays rapidly along the surface normal [51].

To further examine the spoof-LSP mode profiles, we performed spatial mapping experiments on the out-of-plane electric field (E_z) and magnetic field (B_z) components using tip and loop probes, respectively. The probes are custom-made from a coaxial cable assembly with an unterminated end. The diameter of the loop probe is estimated to be ~ 0.8 mm. The probe scans across the resonator plane using a set of precise piezoelectric stages, with a raised height of ~ 1 mm from the surface. The mapping experiments were performed without any YIG sample nor applied magnetic field.

Figure 3(a) and (b) illustrate our measurement setup for mapping E_z (using a tip probe) and B_z (using a loop probe) fields, respectively. Transmission spectra integrated throughout the whole mapped regions were also shown, for each E_z and B_z measurement, next to their setup image. The selective amplification was again confirmed to be localized around 2.6 and 4.2 GHz, consistent with the global transmission characteristics measured earlier. Three representative frequencies, at 2.625 (amplified), 3.765 (not amplified), and 4.195 (amplified) GHz, were selected whose spatial E_z and B_z maps were shown.

For the E_z maps, the 2.625-GHz mode exhibits a twofold symmetry and is a fundamental dipole LSP mode, while the 4.195-GHz mode manifest a fourfold symmetry and corresponds to

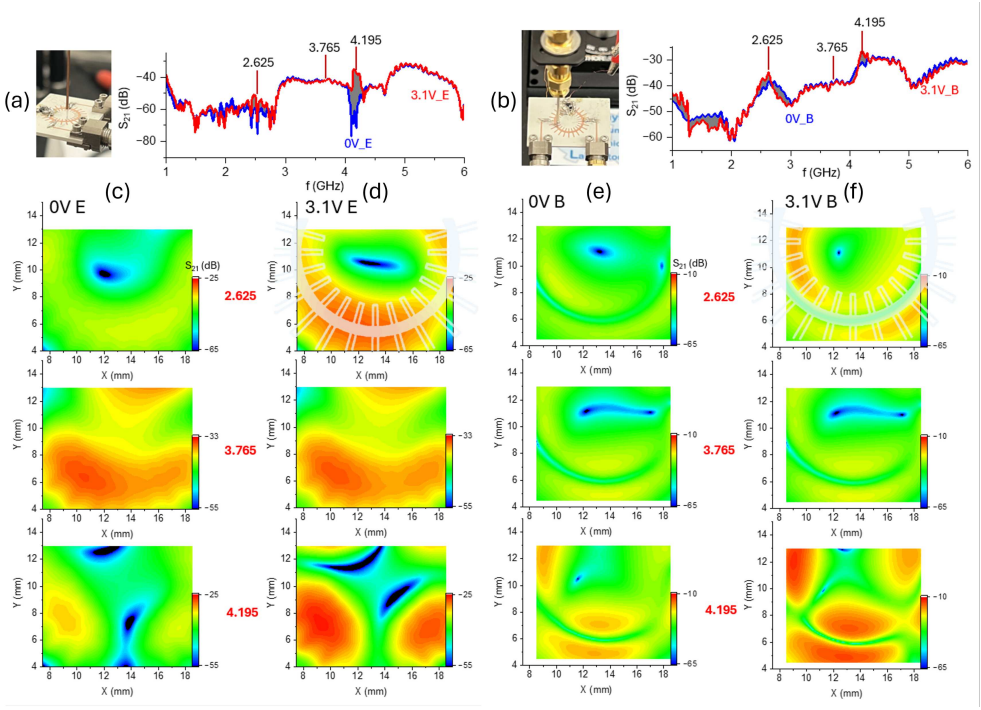

Fig. 3. (a,b) Spatial mapping of the out-of-plane electric and magnetic fields of the spoof-LSP mode without the gain (0 V) and with an intermediate gain (3.1 V) to avoid saturation. (a) Electric field (E_z) mapping using a tip probe and the integrated transmission spectra throughout the whole mapped regions at 0 and 3.1 V. (b) Magnetic field (B_z) mapping using a loop probe and the integrated transmission spectra throughout the whole mapped regions at 0 and 3.1 V. (c,d) Selective (E_z) maps at 2.625, 3.765, and 4.195 GHz: (c) without gain (0 V), and (d) with gain (3.1 V). (e,f) Selective (B_z) maps at 2.625, 3.765, and 4.195 GHz: (e) without gain (0 V), and (f) with gain (3.1 V).

a quadrupole LSP mode. The field amplitude of both modes are significantly bolstered by the gain. As an example, an intermediate transition state at 3.765 GHz was also shown, whose field amplitude, however, remains nearly the same with respect to the additional gain.

Similarly, for the B_z maps, the 2.625-GHz mode exhibits a twofold winding-spiral geometry and is consistent with a fundamental dipole LSP mode. The 4.195-GHz mode manifests a fourfold symmetry and corresponds to a quadrupole LSP mode. In particular, a field hotspot is identified at the bottom of the corrugated ring. Likewise, the field amplitude of both modes are significantly bolstered by the gain. The same intermediate transition state at 3.765 GHz was also shown, indicating a weak susceptibility to the external gain, as in the E_z case.

3.2. Simulation and Modeling

In addition to the experimental measurement results presented in Section II and III, we here provide full wave simulation of the spoof-LSP structure and compare the simulated port responses and field distributions with the measured data, shedding further light on the resonant modes of the spoof-LSP. As shown in Figure 4 (a), a 3D model of the spoof-LSP structure is constructed in Ansys HFSS, including the spoof-LSP resonator, feed lines, amplifier bias layout and all passive circuit elements. The amplifier as an active circuit is not included here. Considering that the resonant behavior of the spoof-LSP is dominated by the passive resonator, and that the active

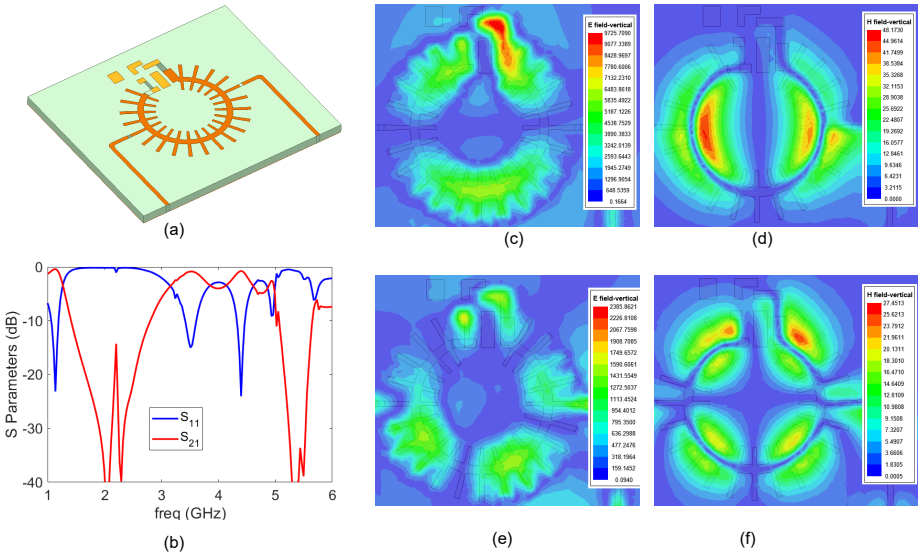

Fig. 4. (a) the 3D model of the spoof-LSP in Ansys HFSS, (b) the two port response from full wave simulation, (c)(d) are the simulated E_z and H_z fields at 2.2 GHz, displaying a dipole resonator response. (e)(f) are the simulated E_z and H_z fields at 4.39 GHz, displaying a quadrupole resonator response.

amplifier only adds loading effects, we expect to see similar resonant behaviors as the measured results.

Figure 4 (b) shows the simulated two-port S parameters of the structure. Several prominent resonant modes within the frequency of interest are identified near 2.2 GHz, 3.51 GHz, and 4.39 GHz, which agree closely with the measured results in Figure 1 (b). To gain more insight on the field distributions of the resonant modes, the vertical E and H fields (namely E_z and H_z) above the spoof-LSP are sampled at a distance of 1mm from the resonator (similar to the measurement probe setup). Figure 4 (c) and (d) shows the E_z and H_z fields at 2.2 GHz, which clearly display a field distribution of a dipole resonator when ignoring the field disruption caused by the amplifier layout circuits. Figure 4 (e) and (f) shows the E_z and H_z fields at 4.39 GHz, and a clear quadrupole resonator response with four-fold symmetry can be identified. The resonance near 3.51 GHz is an anti-resonance due to the combined effect of the dipole and quadrupole resonances, as discussed later in this section. Note that there is slight field disruption near the amplifier region due to layout of the biasing circuits. However, in general, the simulated field distributions at both frequencies (2.2 GHz and 4.39 GHz) agree closely with the measured data at 2.625 GHz and 4.195 GHz in Figure 3. The specific locations of the peaks and nulls in the field distribution could vary due to the loading effects of the amplifier in measurement, but as expected, the resonant behaviors are dominated by the passive spoof-LSP structure.

To better explain the gain-driven resonator mechanism, we further investigated the intrinsic resonance response of the spoof-LSP structure and then combined it with the amplifier circuit and conducted some behavioral level simulation in Keysight ADS. Figure 5 (a) is the simplified LSP structure model in ADS by shorting the DC blocking capacitors in the amplifier layout region. Figure 5 (b) gives the intrinsic input impedance of the LSP resonator structure alone, showing resonances near 2 and 4 GHz, and anti-resonances near 1, 3 and 5 GHz. Such a response can be well represented using the equivalent circuit shown in Figure 5 (c) [53], where multiple series resonance circuits (Z_n) are connected in parallel. Specifically, the lowest order mode Z_0 is

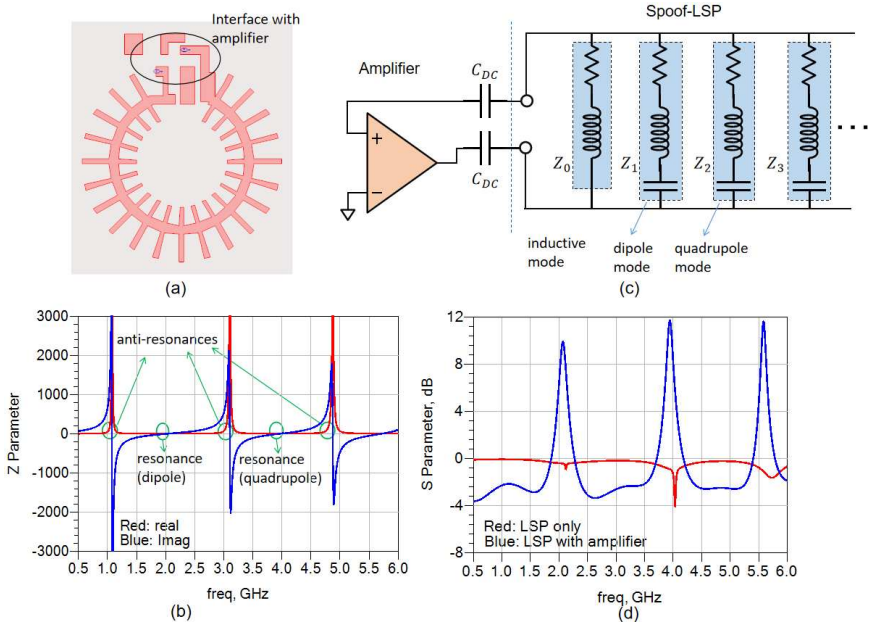

Fig. 5. (a) The simplified LSP structure in ADS; (b) the intrinsic input impedance of the passive LSP structure showing resonances near 2 and 4 GHz and anti-resonances near 1, 3 and 5 GHz (red line for real part and blue line for imaginary part); (c) a representative equivalent circuit of the gain-driven spoof-LSP structure. Z_0 represents the lowest inductive mode (non-resonant); Z_1 represents the dipole mode near 2 GHz and Z_2 represents the quadrupole mode near 4 GHz. The entire spoof-LSP is connected with the input and output of the amplifier forming a positive feedback loop; (d) comparison of the LSP's input responses (S_{11} parameter) without (red line) and with (blue line) the amplifier (a behavioral model is used).

inductive and non-resonant. The 1st resonant mode Z_1 represents the dipole mode near 2 GHz, and the 2nd resonant mode is the quadrupole mode near 4 GHz. Higher order modes can be included if responses at such frequencies are needed. For the gain-driven setup, the LSP structure is connected to the input and output of an amplifier, as shown in Figure 5 (c), forming a positive feedback loop, which is expected to enhance the resonance response. For simple demonstration, a behavioral amplifier is used in ADS for the simulation, with a gain of 13.6 dB, an input resistance of 130 Ohm and an output resistance of 95 ohm, estimated based on the data sheet of our adopted amplifier. Figure 5 (d) compares the LSP's input resonance response (S_{11} of the gain-driven LSP loop) with (blue line) and without (red line) the amplifier. We clearly see boosted oscillation near resonance frequencies due to inclusion of the amplifier. However, the actual resonance response will depend on the gain, input and output impedances (real and imaginary) of the physical amplifier, which are typically frequency dependent. Therefore, the simulation result in Figure 5 (d) only serves to demonstrate the general principle of the gain-driven LSP resonance.

3.3. Photon-magnon coupling properties

Next, we study the photon-magnon coupling behaviors of the gain-assisted spoof-LSP mode. Due to the LSP mode's sensitivity to additional magnetic load, we tested both the YIG sphere (representing minimal magnetic load) and the YIG disc (maximal magnetic load) to investigate the photon-magnon coupling effect. Although the S_{21} measurement can directly manifest the coupling between the stripline and the resonator, the resonator's coupling to YIG can only be

reflected by scanning the magnetic fields and measuring the $f - H$ contour plot. For this purpose, the YIG samples are placed at the bottom of the resonator ring as indicated in Fig.6(a) and (e), respectively. The bias magnetic field is applied along the horizontal direction and scanned across the YIG's Kittel resonance intersecting with the LSP mode. The $f - H$ contour plots at both the 2.6 and 4.2 GHz modes are acquired by detuning the magnetic field near the coupled-mode resonances. The dipolar mode at 2.6 GHz couples much less strongly to the YIG magnon mode compared to the quadrupole mode at 4.2 GHz, therefore, in below we focus on the photon-magnon coupling at the 4.2 GHz mode.

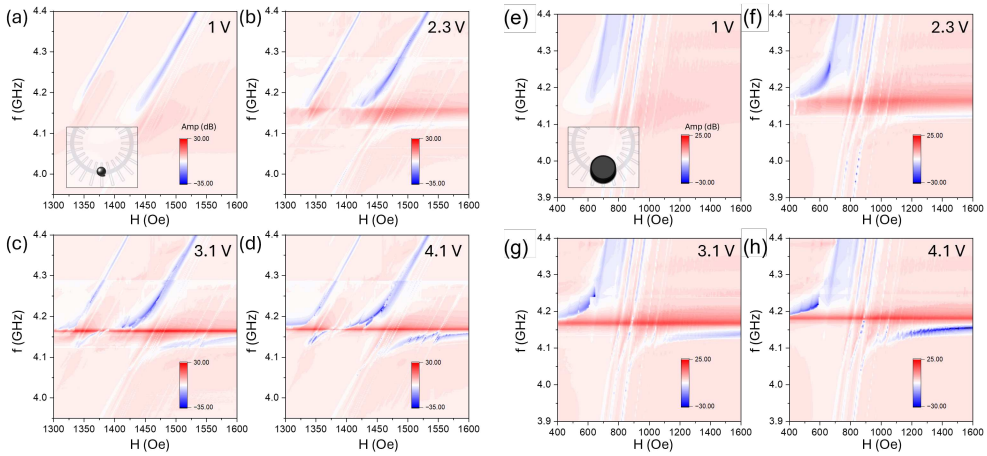

Fig. 6. (a-d) $f - H$ contour plots of the photon-magnon coupling spectra between the quadrupole LSP mode (near 4.2 GHz) and the Kittel magnon mode of a YIG sphere, at different dc-voltage values: (a) 1, (b) 2.3, (c) 3.1, and (d) 4.1 V. (e-h) $f - H$ contour plots of the photon-magnon coupling spectra constructed from dP/df scans after subtracting the initial background. The coupling between the quadrupole LSP mode (near 4.2 GHz) and the Kittel magnon mode of a YIG disc, at different dc-voltage values: (e) 1, (f) 2.3, (g) 3.1, and (h) 4.1 V, are manifested by the anti-crossing features.

Figure 6 shows the photon-magnon coupling spectra of the YIG sphere (a-d) and disc (e-h) samples near their respective Kittel modes at selective dc-voltage (gain) settings, 1, 2.3, 3.1, and 4.1 V. The photon-magnon contour plots are constructed from dP/df scans after subtracting the initial S_{21} background at zero magnetic field. [33, 51] For the YIG sphere, at 1 V or below, the photon mode is still weak, rendering the coupling with the YIG magnon mode nearly negligible; as the gain increases, such as at 2.3 V, an anticrossing gap starts to emerge, indicating the establishment of the photon-magnon hybridization. Due to the slight asymmetry in the development of the photon mode profile versus the gain, see Fig. 1(b), the upper hybridized branch is more prominent than the low hybridized branch.

As the gain further increases, for example at 3.1 V, see Fig.6(c), the photon mode becomes increasingly sharper and the lower branch starts to develop. Above 3.5 V, the coupling strength g ceased to increase further, due to the full establishment of the photon mode profile, see Fig. 7 for a summary of the coupling strength g. However, Further increasing the gain leads to a continuous enhancement of the coupling cooperativity even at the similar size of the anticrossing gap, because the cooperativity, $C = g^2/\kappa_p\kappa_m$, in which κ_p and κ_m are the dissipation rates of the photon and magnon counterparts, respectively [54, 55]. The evolution of the cooperativity against the dc voltage was summarized in Fig.7(b).

At 4.1 V (highest voltage used in the present work), the lower branch becomes strong enough and exhibits further hybridization with additional, higher-order spin-wave modes of the YIG

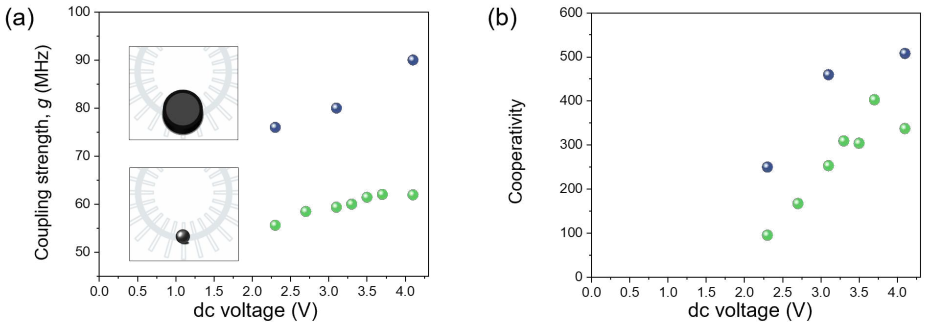

Fig. 7. (a,b) Summary of the dependence of (a) the coupling strength, g, and (b) the cooperativity, C, against the applied dc voltage (gain) for the YIG sphere and disc samples.

sphere. However at the same time, the photon mode dissipation also slightly increased (leading to a corresponding reduction of the cooperativity), possibly due to the convoluted nonlinear couplings between the photon mode and multiple magnon resonances.

Figure 6(e-h) show the corresponding results for the YIG disc, in which the same qualitative features can be observed. Due to the multiple resonances arising in the disc sample, we used only the lower magnon branch for calculating the coupling strength at different dc voltage levels. In Fig.7, we plot the coupling strength and cooperativity, respectively, for the YIG sphere and disc samples, using the pristine linewidths of the YIG magnon and LSP photon modes. Both the coupling and the cooperativity are found larger for the disc sample than with the sphere, primarily due to the larger magnetic volume of the disc matching the spatial mode profile of the spoof-LSP.

Finally, given the fixed spoof-LSP mode profile (e.g. shown in Fig. 3), the in-plane anisotropy of YIG thin films reduces the overall coupling efficiency to the photon mode. Such a coupling would be dependent on the anisotropy strengths, film thicknesses, and the gap distance between the YIG film and the resonator board surface, which would merit a separate study beyond the current parameter space.

4. Summary

To conclude, we designed and fabricated an actively controlled ring resonator accommodating a spoof-LSP mode, and demonstrated gain-assisted photon-magnon coupling with the YIG magnon mode under several different sample geometries. The achieved coupling amplification is largely benefited from the high Q-factors due to the additional gain provided by a semiconductor amplifier, that increases the Q-factor from a nearly null state (passive resonance) to more than 1000 for the quadrupole LSP mode. Our demonstration suggests an additional control knob for manipulating hybrid magnonics, using unconventional surface-plasmon modes leveraging an active amplification effect.

Funding.

The experimental work at UNC-CH and computational work at NCA&T were supported by the U.S. National Science Foundation (NSF) ExpandQISE program under Grant No. ECCS-2426642. S.L. acknowledges support from the NSF under Grant No. DMR-2209427. D.S. acknowledges support from the NSF under Grant No. DMR-2143642. Y.L. acknowledges support by the U.S. Department of Energy, Office of Science, Basic Energy Sciences, Materials Sciences and Engineering Division under Contract No. DE-SC0022060. X.Z. acknowledges support from the NSF under Grant No. ECCS-2337713.

Disclosures.

The authors declare no conflicts of interest.

Data availability.

Data underlying the results presented in this paper may be obtained from the authors upon reasonable request.

References

1. D. D. Awschalom, C. R. Du, R. He, *et al.*, "Quantum engineering with hybrid magnonic systems and materials," IEEE Trans. on Quantum Eng. **2**, 1–36 (2021).
2. D. Lachance-Quirion, Y. Tabuchi, A. Gloppe, *et al.*, "Hybrid quantum systems based on magnonics," Appl. Phys. Express **12**, 070101 (2019).
3. Y. Li, W. Zhang, V. Tyberkevych, *et al.*, "Hybrid magnonics: Physics, circuits, and applications for coherent information processing," J. Appl. Phys. **128** (2020).
4. H. Yuan, Y. Cao, A. Kamra, *et al.*, "Quantum magnonics: When magnon spintronics meets quantum information science," Phys. Reports **965**, 1–74 (2022).
5. B. Flebus, D. Grundler, B. Rana, *et al.*, "The 2024 magnonics roadmap," J. Physics: Condens. Matter (2024).
6. A. V. Chumak, P. Kabos, M. Wu, *et al.*, "Advances in magnetics roadmap on spin-wave computing," IEEE Trans. on Magn. **58**, 1–72 (2022).
7. B. Bhoi and S.-K. Kim, "Photon-magnon coupling: historical perspective, status, and future directions," Solid State Phys. **70**, 1–77 (2019).
8. M. Harder and C.-M. Hu, "Cavity spintronics: An early review of recent progress in the study of magnon–photon level repulsion," Solid State Phys. **69**, 47–121 (2018).
9. M. Goryachev, W. G. Farr, D. L. Creedon, *et al.*, "High-cooperativity cavity qed with magnons at microwave frequencies," Phys. Rev. Appl. **2**, 054002 (2014).
10. X. Zhang, C.-L. Zou, L. Jiang, and H. X. Tang, "Strongly coupled magnons and cavity microwave photons," Phys. review letters **113**, 156401 (2014).
11. Y. Tabuchi, S. Ishino, T. Ishikawa, *et al.*, "Hybridizing ferromagnetic magnons and microwave photons in the quantum limit," Phys. review letters **113**, 083603 (2014).
12. Y.-P. Wang and C.-M. Hu, "Dissipative couplings in cavity magnonics," J. Appl. Phys. **127** (2020).
13. M. Harder, Y. Yang, B. Yao, *et al.*, "Level attraction due to dissipative magnon-photon coupling," Phys. review letters **121**, 137203 (2018).
14. X. Zhang, A. Galda, X. Han, *et al.*, "Broadband nonreciprocity enabled by strong coupling of magnons and microwave photons," Phys. Rev. Appl. **13**, 044039 (2020).
15. Y.-P. Wang, J. Rao, Y. Yang, *et al.*, "Nonreciprocity and unidirectional invisibility in cavity magnonics," Phys. review letters **123**, 127202 (2019).
16. J. Rao, C. Wang, B. Yao, *et al.*, "Meterscale strong coupling between magnons and photons," Phys. Rev. Lett. **131**, 106702 (2023).
17. W.-J. Wu, Y.-P. Wang, J.-Z. Wu, *et al.*, "Remote magnon entanglement between two massive ferrimagnetic spheres via cavity optomagnonics," Phys. Rev. A **104**, 023711 (2021).
18. Y. Li, V. G. Yefremenko, M. Lisovenko, *et al.*, "Coherent coupling of two remote magnonic resonators mediated by superconducting circuits," Phys. Rev. Lett. **128**, 047701 (2022).
19. Y. Xiong, Y. Li, M. Hammami, *et al.*, "Probing magnon–magnon coupling in exchange coupled y 3 fe 5 o 12/permalloy bilayers with magneto-optical effects," Sci. Reports **10**, 12548 (2020).
20. Y. Xiong, J. Inman, Z. Li, *et al.*, "Tunable magnetically induced transparency spectra in magnon-magnon coupled y 3 fe 5 o 12/permalloy bilayers," Phys. Rev. Appl. **17**, 044010 (2022).
21. Y. Xiong, A. Christy, M. Mahdi, *et al.*, "Phase-resolving spin-wave microscopy using infrared strobe light," Phys. Rev. Appl. **22**, 064081 (2024).
22. J. Inman, Y. Xiong, R. Bidthanapally, *et al.*, "Hybrid magnonics for short-wavelength spin waves facilitated by a magnetic heterostructure," Phys. Rev. Appl. **17**, 044034 (2022).
23. J. Qian, C. Meng, J. Rao, *et al.*, "Non-hermitian control between absorption and transparency in perfect zero-reflection magnonics," Nat. Commun. **14**, 3437 (2023).
24. Y. Yang, Y.-P. Wang, J. Rao, *et al.*, "Unconventional singularity in anti-parity-time symmetric cavity magnonics," Phys. Rev. Lett. **125**, 147202 (2020).
25. X. Zhang, K. Ding, X. Zhou, *et al.*, "Experimental observation of an exceptional surface in synthetic dimensions with magnon polaritons," Phys. review letters **123**, 237202 (2019).
26. P. Pirro, V. I. Vasyuchka, A. A. Serga, and B. Hillebrands, "Advances in coherent magnonics," Nat. Rev. Mater. **6**, 1114–1135 (2021).
27. A. Serga, A. Chumak, and B. Hillebrands, "Yig magnonics," J. Phys. D: Appl. Phys. **43**, 264002 (2010).
28. G. Gubbiotti, A. Barman, S. Ladak, *et al.*, "2025 roadmap on 3d nano-magnetism," J. Physics: Condens. Matter (2024).
29. H. Merbouche, B. Divinskiy, D. Gouéré, *et al.*, "True amplification of spin waves in magnonic nano-waveguides," Nat. Commun. **15**, 1560 (2024).

30. D. Breitbach, M. Schneider, B. Heinz, *et al.*, "Stimulated amplification of propagating spin waves," Phys. Rev. Lett. **131**, 156701 (2023).
31. J. Qian, P. Gou, Y. Gui, *et al.*, "Plasmonic diabolo cavity enhanced spin pumping," Appl. Phys. Lett. **111** (2017).
32. H. Pan, J. Qian, Z. Rao, *et al.*, "Spin pumping of magnons coherently coupled to a cavity dark mode," Phys. Rev. Appl. **19**, 014075 (2023).
33. Y. Xiong, A. Christy, Y. Dong, *et al.*, "Combinatorial split-ring and spiral metaresonator for efficient magnon-photon coupling," Phys. Rev. Appl. **21**, 034034 (2024).
34. J. Xu, C. Zhong, S. Zhuang, *et al.*, "Slow-wave hybrid magnonics," Phys. Rev. Lett. **132**, 116701 (2024).
35. Y. Li, T. Polakovic, Y.-L. Wang, *et al.*, "Strong coupling between magnons and microwave photons in on-chip ferromagnet-superconductor thin-film devices," Phys. review letters **123**, 107701 (2019).
36. J. T. Hou and L. Liu, "Strong coupling between microwave photons and nanomagnet magnons," Phys. review letters **123**, 107702 (2019).
37. C. Zhang, M. Kim, J. Wang, and C.-M. Hu, "Van der pol–duffing oscillator and its application to gain-driven light-matter interaction," Phys. Rev. Appl. **22**, 014034 (2024).
38. Y. Xiong, J. M. Nair, A. Christy, *et al.*, "Magnon-photon coupling in an opto-electro-magnonic oscillator," npj Spintron. **2**, 9 (2024).
39. Y. Xiong, Z. Zhang, Y. Li, *et al.*, "Experimental parameters, combined dynamics, and nonlinearity of a magnonic-opto-electronic oscillator (moeo)," Rev. Sci. Instruments **91** (2020).
40. B. Yao, Y. Gui, J. Rao, *et al.*, "Coherent microwave emission of gain-driven polaritons," Phys. Rev. Lett. **130**, 146702 (2023).
41. C. Zhang, M. Kim, Y.-H. Zhang, *et al.*, "Gain-loss coupled systems," arXiv preprint arXiv:2410.20338 (2024).
42. Y. Yang, J. Yao, Y. Xiao, *et al.*, "Anomalous long-distance coherence in critically driven cavity magnonics," Phys. Rev. Lett. **132**, 206902 (2024).
43. F. J. Garcia-Vidal, A. I. Fernández-Domínguez, L. Martin-Moreno, *et al.*, "Spoof surface plasmon photonics," Rev. Mod. Phys. **94**, 025004 (2022).
44. P. A. Huidobro, X. Shen, J. Cuerda, *et al.*, "Magnetic localized surface plasmons," Phys. Rev. X **4**, 021003 (2014).
45. X. Zhang, W. Y. Cui, Y. Lei, *et al.*, "Spoof localized surface plasmons for sensing applications," Adv. materials technologies **6**, 2000863 (2021).
46. B. J. Yang, Y. J. Zhou, and Q. X. Xiao, "Spoof localized surface plasmons in corrugated ring structures excited by microstrip line," Opt. express **23**, 21434–21442 (2015).
47. Z. Gao, F. Gao, K. K. Shastri, and B. Zhang, "Frequency-selective propagation of localized spoof surface plasmons in a graded plasmonic resonator chain," Sci. reports **6**, 25576 (2016).
48. Z. Liao, S. Liu, H. F. Ma, *et al.*, "Electromagnetically induced transparency metamaterial based on spoof localized surface plasmons at terahertz frequencies," Sci. reports **6**, 27596 (2016).
49. J. Cai, Y. J. Zhou, Y. Zhang, and Q. Y. Li, "Gain-assisted ultra-high-q spoof plasmonic resonator for the sensing of polar liquids," Opt. express **26**, 25460–25470 (2018).
50. Q. Y. Li, X. Zhao, H. Z. Zhao, and Y. J. Zhou, "Selective amplification of spoof localized surface plasmons," Appl. Opt. **58**, 9797–9802 (2019).
51. Y. Xiong, A. Christy, Z. Yan, *et al.*, "Hybrid magnonics with localized spoof surface-plasmon polaritons," Phys. Rev. Appl. **22**, 034009 (2024).
52. D. Wagle, A. Rai, M. T. Kaffash, and M. B. Jungfleisch, "Controlling magnon-photon coupling in a planar geometry," J. Physics: Mater. **7**, 025005 (2024).
53. A. F. McKinley, T. P. White, I. S. Maksymov, and K. R. Catchpole, "The analytical basis for the resonances and anti-resonances of loop antennas and meta-material ring resonators," J. Appl. Phys. **112**, 094911 (2012).
54. J. Bourhill, N. Kostylev, M. Goryachev, *et al.*, "Ultrahigh cooperativity interactions between magnons and resonant photons in a yig sphere," Phys. Rev. B **93**, 144420 (2016).
55. K. Kato, R. Sasaki, K. Matsuura, *et al.*, "High-cooperativity cavity magnon-polariton using a high-q dielectric resonator," J. Appl. Phys. **134** (2023).